Thermoreversible gels composed of colloidal silica rods with short-range attractions

Ryan P. Murphy,[†] Kunlun Hong,[‡] Norman J. Wagner[†]*

† Center for Molecular and Engineering Thermodynamics & Center for Neutron Science, Department of Chemical and Biomolecular Engineering, University of Delaware, Newark, Delaware 19716, United States

‡ Center for Nanophase Materials Sciences, Oak Ridge National Laboratory, Oak Ridge, Tennessee 37831, United States

ABSTRACT

Dynamic arrest transitions of colloidal suspensions containing non-spherical particles are of interest for the design and processing of various particle technologies. To better understand the effects of particle shape anisotropy and attraction strength on gel and glass formation, we present a colloidal model system of octadecyl-coated silica rods, termed as adhesive hard rods (AHR), which enables control of rod aspect ratio and temperature-dependent interactions. The aspect ratios of silica rods were controlled by varying the initial TEOS concentration following the work of Kuijk *et al.* (*J. Am. Chem. Soc.*, 2011) and temperature-dependent attractions were introduced by coating the calcined silica rods with an octadecyl-brush and suspending in tetradecane. The rod length and aspect ratio were found to increase with TEOS concentration as expected, while other properties such as the rod diameter, coating coverage, density, and surface roughness were nearly independent of the aspect ratio. Ultra-small angle X-ray scattering measurements revealed temperature-dependent attractions between octadecyl-coated silica rods in tetradecane, as characterized by a low-q upturn in the scattered intensity upon thermal quenching. Lastly, the rheology of a concentrated AHR suspension in tetradecane demonstrated thermoreversible gelation behavior, displaying a nearly five order of magnitude change in the dynamic moduli as the temperature was cycled between 15 °C and 40 °C. The adhesive hard rod model system serves as a tunable platform to explore the combined influence of particle shape anisotropy and attraction strength on the dynamic arrest transitions in colloidal suspensions with thermoreversible, short-range attractions.

1. INTRODUCTION

Suspensions of anisotropic or non-spherical colloids such as clays, proteins, carbon nanotubes, graphene, cellulose nanocrystals, and other inorganic mineral crystals are widely used in particle technologies such as pharmaceuticals, consumer products, composites, paints, coatings, and cements. The dynamic arrest transitions of colloidal suspensions, or formation of gels and glasses, have been studied extensively for experimental model systems containing attractive spherical colloids,[1,2,3,4] and to a lesser extent for systems containing attractive anisotropic colloids.[5,6,7,8] An improved understanding of dynamic arrest transitions and the effects of particle shape anisotropy remains an important paradigm in particle technology design and manufacturing process that employ anisotropic particle suspensions.

Recently, a water-in-oil emulsion method was developed to synthesize rod-like silica colloids with tunable aspect ratios within the range of 1-25 and with narrow size distributions.[9] These rod-like silica colloids have been used as a model system to explore phase behavior,[10,11] crystal transitions in confinement,[12] and directed field assembly[13,14] of hard spherocylinders with repulsive interactions. Moreover, the emulsion method to produce rod-like silica colloids has shown unique versatility by introducing other shape facets such as segmented ridges,[15,16] bends,[17] spikes,[18] fibers,[19] site-specific growth with gold ends[20] or PMMA ends,[21] and "match stick" colloids with manganese oxide or iron oxide.[22] Building upon these synthetic approaches, we present a model system of adhesive hard rods (AHR) by introducing temperature-dependent, short-range attractions afforded by octadecyl-coated silica dispersed in organic solvents.

Chemically grafting an octadecyl-brush onto the surface of silica spheres[23] has been shown to produce thermoreversible gels when suspended in organic solvents such as benzene,[24] n-hexadecane,[25,26] and n-tetradecane.[27] When suspended in tetradecane, octadecyl-coated silica

spheres exhibit a thermoreversible gel transition from a fluid-like to a solid-like state upon cooling from 40 °C to 20-30 °C, depending on the particle volume fraction.[3] The fluid-state can be recovered by heating the sample to 40 °C, which enables a convenient methodology to thermally cycle between the two states to better quantify the gelation behavior. Arrested states were shown to arise from a surface freezing and melting effect, whereby the linear alkane solvent interdigitates and crystallizes with the surface-grafted brush, leading to a short-range attraction between particles.[25, 27, 28] This experimental model system has been used to map the gelation boundary, or rigidity percolation boundary, onto a fundamental colloidal state-diagram for adhesive hard spheres (AHS) with short-range attractions as a function of attraction strength and volume fraction.[4] Neutron scattering and rheological methods were used to map the gelation boundary of AHS, in which the sticky spheres were found to percolate into a homogeneous network structure. Dynamic arrest of AHS was later shown to correspond to rigidity percolation using computer simulations.[29] The stability of such gels at low volume fractions was limited by gravitational settling,[30] and a continuous transition from gelation to an attractive driven glass was observed.[3]

Herein, we extend this methodology to incorporate thermoreversible short-range attractions into rod-shaped silica colloids to produce adhesive hard rods with tunable aspect ratios and attraction strength. We extend the previous work by Kuijk *et al.* by confirming the length and aspect ratio of silica rods can be tuned by adjusting the addition of the silica precursor, tetraethyl orthosilicate (TEOS).[9] Temperature-sensitive attractions between silica rods are subsequently introduced by calcining and then coating silica rods with an octadecyl-brush.

Synthesis of the AHR system followed three main steps, as depicted schematically in Fig. 1. First, silica rods were synthesized from water-in-oil emulsion following Kuijk *et al.*[9] Second, the silica rods were calcined at 500 °C to remove entrapped polymer and other residual organics within

the porous silica structure. Third, the calcined silica rods were coated with an octadecyl-brush following van Helden *et al*. to enable suspension in organic solvents such as tetradecane.[23] Adhesive hard rods were characterized with electron microscopy, ultra-small angle X-ray scattering, and other analytical methods to quantify particle shape, size, polydispersity, density, surface area, coating coverage, and surface roughness. Finally, the rheology of a concentrated suspension of AHR in tetradecane was shown to exhibit thermoreversible gelation behavior near room temperature. The adhesive hard rod model system enables exploration into the combined influence of particle shape anisotropy and attraction strength on dynamic arrest transitions.
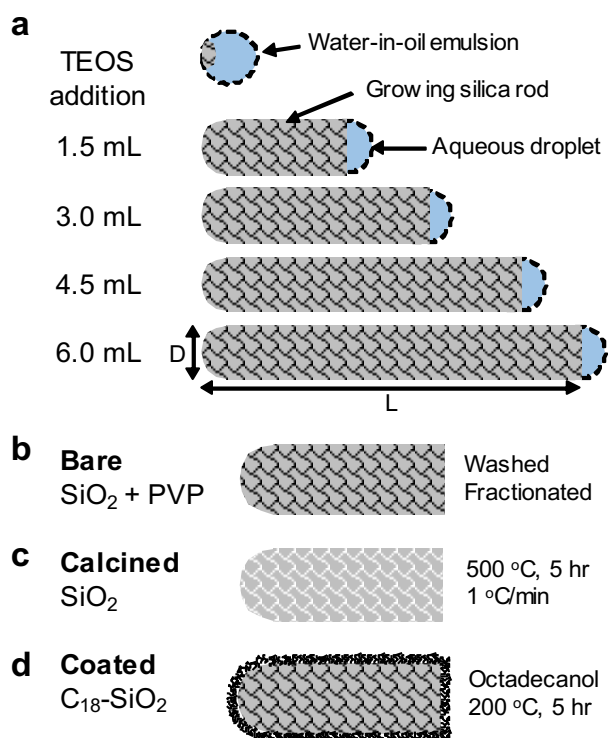

Figure 1. Schematic for synthesis of adhesive hard rods composed of octadecyl-coated silica rods. (a) TEOS addition was varied for the same initial water-in-oil emulsion, producing primary growth along the particle length axis (L) and significantly less growth in the diameter (D). The resulting particle has a hemispherocylinder shape with one hemispherical end and one flat end, which is referred to as "rod" for simplicity. (b) Bare silica rods contain residual organics such as PVP after

separation, washing, and fractionation. (c) Calcination of bare silica rods can be used to remove residual organics. (d) Coated silica rods are produced by chemically grafting an octadecyl-brush ($\sim$2 nm)[27] onto the surface of calcined silica rods (D $\sim$ 250-300 nm, L $\sim$ 700-2000 nm) to enable dispersion in organic solvents such as tetradecane.

2. MATERIALS AND METHODS

2.1 Silica rod synthesis

Rod-shaped silica colloids were synthesized according to previously described methods.[9] For a given batch, 30 g of polyvinylpyrrolidone (PVP, 40 kg mol^{-1}, Sigma Aldrich) was mixed with 300 mL of 1-pentanol (99%, ACROS Organics) in a clean 1 L HDPE bottle and bath sonicated (Fisher Scientific FS60H, 100 W, 42 kHz) for 1-2 h. Subsequently, 30 mL of ethanol (200 proof, Decon Labs) and 8.4 mL of water (18.2 MΩ-cm) were added, and the mixture was shaken manually for 1 min. Next, 2 mL of 0.18 M aqueous sodium citrate dihydrate (Fisher Scientific) was added and shaken for 1 min, followed by the addition of 6.75 mL of ammonia (25 wt%, Merck), which was further shaken for 1 min. Finally, a defined amount of tetraethyl orthosilicate (TEOS, 98%, ACROS Organics) was added drop-wise to the mixture, and the mixture was shaken for 10 s. The volume of TEOS added in a single step to each batch ranged from 1.5 mL, 3 mL, and 4.5 mL to produce silica particles with smaller or larger average aspect ratios, respectively. When adding a total of 6 mL of TEOS, first 3 mL of TEOS was added to the mixture and then allowed to react unperturbed for 6 h. Afterwards, the additional 3 mL TEOS was added, gently rotated to distribute, and then allowed to react for an additional 12-18 h. Importantly, the mixture was allowed to react unperturbed without stirring. Stirring during the reaction was previously shown to disrupt the rod growth by destabilizing the adsorbed water droplet on the flat-end, which effectively terminates

the nearly one-dimensional growth of the silica rod.[9] Approximately 5-10 g of silica rods were produced by combining 10-20 identical batches in parallel.

2.2 Particle washing and fractionation

Silica particles were separated from the emulsion mixture through a series of washing and centrifugation steps. First, the emulsion mixture was centrifuged at 3000 g for 60 min, and the supernatant was discarded. The silica particles were resuspended in ethanol with bath sonication and vortex mixing (3000 rpm). The suspension was then centrifuged again at 3000 g for 30 min, and the supernatant was discarded. The washing and centrifugation process was repeated twice more with ethanol, and twice more using water to remove excess PVP. After washing, silica particles were fractionated through a series of further centrifugation steps in ethanol. The suspension was centrifuged a total of 3 times at 700 g for 15 min each, discarding the supernatant each time. An additional single fractionation step was performed at 100 g for 5 min to remove larger rods and aggregates. In this last step, the bottom sediment was discarded and supernatant was collected. Particles were dried under air and stored until subsequent calcination and coating steps. Typically, ~0.4 g of bare silica or ~50% of the maximum yield was recovered per batch with 3 mL TEOS added.

2.3 Calcination

The fractioned bare silica particles were calcined to remove residual polymer (PVP) and other organics that remained trapped within the porous silica network, which could influence the subsequent octadecyl-brush coating step and short-range attraction in organic solvents. The majority of organic material removed was assumed to be PVP, based on the significant loss in mass after dehydration and thermal degradation (8-12 wt%). Dried bare silica particles were transferred to a ceramic crucible and calcined in air at 500 °C (1 °C/min ramp up) for 5 h. Calcined

particles were then suspended in 4:1 v/v ethanol/water mixture by sonication and vortex mixing. The suspension was centrifuged at 3000 g for 15 min and resuspended in pure ethanol for the subsequent octadecyl-brush coating step.

2.4 Octadecyl-brush coating

Calcined silica particles were coated with an octadecyl-brush following the method by van Helden *et al.* to enable dispersion in organic solvents.[23] Briefly, 1-octadecanol (97%, Alfa Aesar) was added in excess to a suspension of calcined silica rods in ethanol at a ratio of 6:1 w/w octadecanol/silica in a round bottom flask. The reaction mixture was continuously rotated and heated in an oil bath, while water and ethanol were condensed using a water-cooled overhead condenser. The mixture was slowly heated to 110-120 °C to remove ethanol and water, slowly heated to 200 °C (1 °C/min), and then allowed to react for 5 h. The mixture was cooled to room temperature, and the solids were suspended and washed with approximately 425 mL of 3:2 v/v chloroform/cyclohexane mixture. The coated particles were collected by centrifugation at 6000 g for 60 min, collecting the sediment after each wash. The octadecyl-coated silica rods were washed 3 times with the chloroform/cyclohexane mixture and once more with pure cyclohexane. Coated silica rods were stored in cyclohexane at room temperature until further use. The octadecyl-brush and organophilic properties of coated silica rods appeared stable for at least 5 months, based on consistent rheological measurements of AHR suspensions in tetradecane. It was previously reported that the octadecyl-brush layer on organophilic silica spheres remained unchanged for more than 2 years when stored in organic solvents such as cyclohexane, while prolonged storage in air could cause hydrolysis or oxidation of the coating layer.[23]

2.5 Gel preparation

Octadecyl-coated silica rods were suspended in tetradecane to form a thermoreversible gel. Coated silica particles suspended in cyclohexane were dried under a nitrogen stream before further drying under vacuum at 50 °C for 10-12 hours. The dried particles were immediately weighed and suspended in tetradecane (99%, Fisher Scientific) at a specified weight fraction. The suspensions were heated in an oven at 40 °C and initially vortex mixed to promote dispersion. The particle volume fraction of coated silica rods in tetradecane was estimated using the calcined particle skeletal density (2.08 ± 0.02 g/cm^3), the mass fraction of the brush determined by TGA (4.3 ± 0.7 wt%), the estimated brush density in the fluid state using octadecane (0.777 g/cm^3 at 30 ºC),[31] and tetradecane density (0.763 g/cm^3).

2.6 Scanning and transmission electron microscopy (SEM and TEM)

Particle size distributions were determined using a Zeiss Merlin SEM operating at 1 kV and 100 pA and using mixed signal from SE2 and InLens detectors. Images were captured with noise reduction by line-averaging over 30-60 s. Samples were prepared by pipetting 3 μL of sample directly onto a clean silicon wafer and dried in air. Particle dimensions were analyzed with ImageJ software to obtain the mid-point diameter (D), total end-to-end length (L), and aspect ratio (AR = L/D). Approximately 200 particles were analyzed for each sample to determine the particle size statistics and distributions of L, D, and AR.

Surface roughness along the particle edge was visualized by TEM using a Zeiss Libra 120 and a FEI Tecnai G2 Twin instruments operating at 120 kV and 3 μA. Images were captured with a Gatan CCD camera. Samples were prepared by pipetting 3 μL onto a clean carbon-coated copper grid and dried in air. The surface height (h, perpendicular to the length axis) was traced along a 150-200 nm line-segment as measured along an edge of a particle (x, length axis). The particle

edge was traced to produce a surface profile relative to a perfectly flat edge. Surface roughness parameters, including the root mean squared height and the maximum peak height, were averaged from surface profiles obtained from at least three different particles for each sample.

2.7 Ultra-small angle X-ray scattering (USAXS)

USAXS experiments were performed on the 9-ID-C beamline at the Advanced Photon Source at Argonne National Laboratory.[32] The incident X-ray beam consisted of wavelength $\lambda = 0.689$ Å (18 keV) and a beam size of 0.5 mm x 2 mm. Samples were loaded into glass capillaries (KIMAX, average 1.25 mm ID, 1.5-1.8 mm OD) and were sealed with wax to prevent solvent evaporation. Sample temperature was measured with a calibrated temperature probe ($\pm$ 0.1 °C) and was controlled using a custom-built, multi-sample, aluminium capillary cage in connection with a temperature-controlled water bath. (Stage is available for public use). The slit-smeared scattered intensity (slit length = 0.0282 Å^{-1}) was collected over 120 s, spanning a q-range of 0.0001 Å$^{-1} < q < 1$ Å^{-1}, where q is the scattering wave vector defined as $q = 4\pi\lambda^{-1}\sin(\theta/2)$, and θ is the scattering angle. Scattering from the empty capillary cell was subtracted using the standard reduction and analysis procedures provided in the Indra, Irena, and Nika software packages.[33, 34] USAXS scattering data of dilute silica rods were fit using a polydisperse cylinder form factor model[35, 36] using a Schulz distribution in the length and radius (see Supporting Information), as implemented in the SasView software package v3.1.2.[37]

2.8 Specific surface area

The specific surface area for bare and calcined silica rods was determined from N_2 adsorption measurements and Brunauer-Emmett-Teller (BET) analysis using a Micrometrics Gemini or ASAP 2020 instrument performed at -196 °C. Samples were dried under vacuum at 120 °C for several hours before each measurement to remove residual water. The BET specific surface area

(S_{BET}) was determined from linear regression of a typical adsorption isotherm (BET plot) within a range of reduced pressure (P/P_0) from 0.05 to 0.3.[38] The exterior geometric specific surface area (S_g) was estimated using the average D and L determined from SEM, the particle density, the average particle volume, and assuming a hemispherocylinder particle shape.

2.9 Thermogravimetric analysis (TGA)

TGA was performed using a TA Instruments Q500 to determine the mass fraction of residual PVP and other organics contained within bare, calcined, and coated silica rods. Temperature ramping protocols were consistent for each sample: (1) ramp to 120 °C at 5 °C/min; (2) isothermal hold at 120 °C for 30 min to remove residual water or solvent; (3) ramp to 500 °C at 5 °C/min; (4) isothermal hold at 500 °C for 60 min; (5) cool to room temperature. The samples were purged with nitrogen at 20 mL/min.

The mass fraction of the octadecyl-brush layer on coated silica rods was estimated according to Eq. (1), which is derived from a mass balance, and TGA measurements of the mass loss after thermal degradation at 500 °C. The mass fraction of the octadecyl-brush grafted on coated silica rods m_b is given as

$$m_b = \frac{(w_{calcined} - w_{coated})}{(w_{calcined} - w_{brush})} \quad (1)$$

in which, $w_{calcined}$ is the remaining fractional mass of the calcined silica rods after thermal degradation, w_{brush} is the remaining fractional mass of octadecanol after degradation (w_{brush} = 0.004), and w_{coated} is the remaining fractional mass of coated silica particles after degradation.

The coating coverage, or number of grafted octadecyl-chains per surface area of coated silica rods, was estimated according to Eq. (2), given as

$$n = \frac{m_b N_A}{(1 - m_b) S M_o} \quad (2)$$

in which n is the number of chains per area, S is the specific surface area of calcined silica rods, M_o is the assumed molecular weight of the brush (using octadecane, 254.5 g mol^{-1}), and N_A is Avogadro's constant. The best estimate of coating coverage employed the specific surface area determined from BET analysis (0.9-1.4 chains/nm^2). The estimated coating coverage using the geometric surface area (7.1-8.5 m^2/g) provided physically unrealistic coating coverages (13-16 chains/nm^2), which shows that the coating can penetrate into the particle's pores.

2.10 Particle skeletal density

Particle skeletal density was determined using an Anton Paar DMA 4500 oscillating U-tube density meter. Dried calcined and bare silica rods were suspended in water at concentrations between 0.1 – 2.5 wt%, while coated silica rods were suspended in cyclohexane. The suspension density was measured after equilibration at 25 °C. The particle skeletal density, which measures the density of the particle defined as the solid plus any internal pores not accessible to the solvent and does not account for the volume of solvent within solvent-accessible pores , was calculated under the assumption of ideal mixing using:

$$\frac{1}{\rho_s} = \left(\frac{1}{\rho_p} - \frac{1}{\rho_m}\right)x_p + \frac{1}{\rho_m} \quad (3)$$

in which ρ_s is the measured suspension density, ρ_m is the measured medium (solvent) density, ρ_p is the unknown particle skeletal density, and x_p is the measured particle mass fraction determined from the dried powder.

2.11 Rheological characterization

Small amplitude oscillatory shear measurements were performed using a TA Instruments DHR-3 rheometer operating in stress-controlled mode with a cone-plate geometry (40 mm cone diameter, 1° cone angle) and a temperature-controlled Peltier plate (± 0.01 °C). A solvent trap was used to limit evaporation of tetradecane and to reduce thermal gradients in the sample during

measurements, both of which were determined to be negligible during the course of the experiments reported here.

Each rheological measurement followed a specific pre-shear protocol to maintain sample consistency, to erase the shear history of the sample, and to recover the initial fluidized state. The pre-shear protocol included: (1) heating sample to 40 °C and shearing at a shear rate of 10 s^{-1} for 2 min, and (2) cooling to temperature of interest and equilibrating for 5 min at rest. The steady-shear viscosity at 40 °C was monitored between measurements to check for sample consistency before and after each measurement. Due to the density mismatch between particles and tetradecane, sedimentation effects were apparent on the timescale of hours and were evident as a slow decrease in the steady-shear viscosity at 40 °C. The sample could be successfully resuspended by shearing at 20 s^{-1} for 2 min in the gel-state at 20 °C, followed by the initial pre-shear protocol at 40 °C described previously. By implementing this additional shear step, the steady-shear viscosity at 40 °C was consistent for at least 48 h of thermal cycling and testing.

After pre-shearing, temperature sweeps in the cooling and heating direction were performed between 35 °C and 15 °C at a ramp rate of 1 °C/min, a stress amplitude of $\sigma_0 = 30$ mPa, and a frequency $\omega = 1$ Hz. Due to the large changes in dynamic moduli upon cooling and heating the sample, signal-to-noise was improved at temperatures below the gel transition (15-25 °C) by repeating the temperature ramp at a small strain amplitude of $\gamma_0 = 0.01\%$. Stress amplitude sweeps were performed from $\sigma_0 = 0.006$ to 6 Pa (torque = 0.1 to 100 µN-m) at constant temperature and frequency of 1 Hz. Frequency sweeps were performed from 0.1 to 10 rad/s at a constant temperature and minimum stress amplitude of $\sigma_0 = 30$ mPa within the linear viscoelastic regime.

3. RESULTS AND DISCUSSION

The general scheme for synthesizing adhesive hard rods (AHR) composed of octadecyl-coated silica rods is shown schematically in Fig. 1. By controlling the concentration of TEOS, the length of the silica rod can be increased without significant increase in the rod diameter, providing a method to control the average particle aspect ratio. In principle, this method can be extended to produce AHR with desirable aspect ratios within the range of 1-25.[9] The silica rods were calcined to remove residual organics trapped within the silica network. After calcination, particles were coated with an octadecyl-brush and suspended in tetradecane to introduce temperature-dependent attractions and to demonstrate thermoreversible gelation behavior.

For reference, the sample name (AR3, AR4, AR6, AR7) corresponds to the average aspect ratio determined from SEM measurements. The notation "bare" refers to rods that were washed and fractionated by centrifugation; "calcined" refers to rods that were calcined at 500 °C to remove residual polymer; "coated" refers to rods that were grafted with an octadecyl-brush to allow suspension in organic solvents. Table 1 summarizes particle characteristics in this work, including the average particle diameter (D), length (L), aspect ratio (AR = L/D), standard deviations of diameter (σ_D), length (σ_L), and aspect ratio (σ_{AR}), particle skeletal density (ρ_p), specific BET and geometric surface area (S_{BET} and S_g), mass loss after thermal degradation (w), grafted octadecyl-brush mass fraction (m_b), coating coverage (n), and surface roughness.

Table 1. Summary of particle sizes and properties for bare, calcined, and coated silica rods

Name	TEOS (mL/batch)	Diameter (nm)	Length (nm)	Aspect ratio	Density (g/cm^3)	Surface area (m^2/g)	TGA mass loss (wt%)	Brush mass (wt%)	Coating coverage (chains/nm^2)	Surface roughness (nm)
AR3 bare	1.5	252 ± 33	681 ± 111	2.7 ± 0.2	-	-	8.4 ± 1.0%	-	-	-
AR3 calcined	-	[a]266 ± 39 [b]264 ± 58	[a]691 ± 79 [b]841 ± 126	[a]2.6 ± 0.3 [b]3.2 ± 0.8	2.08 ± 0.02	[c]78 ± 4 [d]8.5	0.7 ± 0.5%	-	-	[e]1.3 ± 0.3 [f]3.9 ± 0.9
AR3 coated	-	[a]259 ± 37	[a]700 ± 76	[a]2.7 ± 0.3	-	-	4.9 ± 0.5%	4.3 ± 0.7%	1.4 ± 0.3	-
AR4 bare	3.0	261 ± 35	1034 ± 261	3.9 ± 0.6	1.82 ± 0.01	64 ± 3	9.2 ± 0.9%	-	-	-
AR4 calcined	-	[a]269 ± 36 [b]261 ± 54	[a]1123 ± 251 [b]1201 ± 341	[a]4.2 ± 0.7 [b]4.6 ± 1.6	2.08 ± 0.01	[c]128 ± 7 [d]7.9	1.3 ± 0.5%	-	-	[e]1.6 ± 0.6 [f]4.8 ± 1.8
AR4 coated	-	258 ± 43	1099 ± 252	4.2 ± 0.7	1.79 ± 0.14	-	6.2 ± 0.5%	5.0 ± 0.7%	1.0 ± 0.2	-
AR6 bare	4.5	258 ± 37	1488 ± 566	5.7 ± 1.7	-	-	11.9 ± 0.5%	-	-	-
AR6 calcined	-	[a]257 ± 44 [b]252 ± 67	[a]1553 ± 537 [b]1684 ± 264	[a]5.9 ± 1.4 [b]6.7 ± 2.1	2.12 ± 0.01	[c]137 ± 9 [d]7.9	1.2 ± 0.5%	-	-	[e]1.1 ± 0.3 [f]2.7 ± 0.7
AR6 coated	-	252 ± 36	1502 ± 512	5.9 ± 1.6	-	-	5.9 ± 0.5%	4.8 ± 0.7%	0.9 ± 0.2	-
AR7 bare	6.0	295 ± 55	1925 ± 742	6.5 ± 2.2	-	-	11.3 ± 0.5%	-	-	-
AR7 calcined	-	[a]286 ± 57 [b]299 ± 76	[a]2006 ± 709 [b]2032 ± 727	[a]6.9 ± 1.9 [b]6.8 ± 3.0	-	[c]69 ± 1 [d]7.1	1.7 ± 0.5%	-	-	[e]1.2 ± 0.2 [f]2.8 ± 0.5
AR7 coated	-	298 ± 65	2019 ± 747	6.8 ± 2.1	-	-	5.6 ± 0.5%	4.0 ± 0.7%	1.4 ± 0.3	-

Values are given as the mean ± standard deviation. [a] Size determined from SEM; [b] Best fit size from USAXS using the polydisperse cylinder form factor model; [c] Surface area from BET analysis; [d] Geometric surface area of hemispherocylinder shape using dimensions from SEM; [e] Root mean squared height from TEM profiles; [f] Maximum height from TEM profiles

3.1 Particle shape and size distributions

Kuijk *et al*. provided convincing evidence that the primary growth mechanism of silica rods relied on the stability of a terminal water droplet adsorbed on the growing silica rod.[9] A higher concentration of critical reagents within the terminal aqueous droplet enabled growth primarily along the length axis, with significantly less growth along the radial axis. The residual flat silica end manifests as the rod growth becomes terminated due to removal of the terminal water droplet, presumably after shear or dilution. The resulting hemispherocylinder particle shape, referred to as a rod for simplicity, is in stark contrast to monodisperse silica spheres produced by the Stöber method in which siloxane clusters nucleate and grow in a surface-limited reaction.[39,40] The water-in-oil emulsion method has been shown to produce silica rods with relatively narrow size distributions after fractionation steps with good reproducibility and shape adaptability.[9, 11, 15, 16, 18, 22] The apparent rod length depends on the stability of the end-terminal water droplet, the TEOS concentration, the diffusivity of reagents from the organic phase to the aqueous phase, and the rate of hydrolysis and condensation reactions within the terminal aqueous droplet. The apparent rod diameter generally follows the initial emulsion diameter, and therefore, is not expected to depend strongly on the TEOS concentration.

Figure 2 shows SEM images of coated silica rods produced from the addition of (a) 1.5 mL, (b) 3 mL, (c) 4.5 mL, and (d) 6 mL TEOS to the same initial emulsion composition, which are referred to as AR3, AR4, AR6, and AR7, respectively, based on the average aspect ratio determined from SEM. There were no distinct differences in rod dimensions between the bare, calcined, and coated rods, which confirmed that the implemented calcination and coating steps did not significantly alter the silica rod dimensions (Table 1).
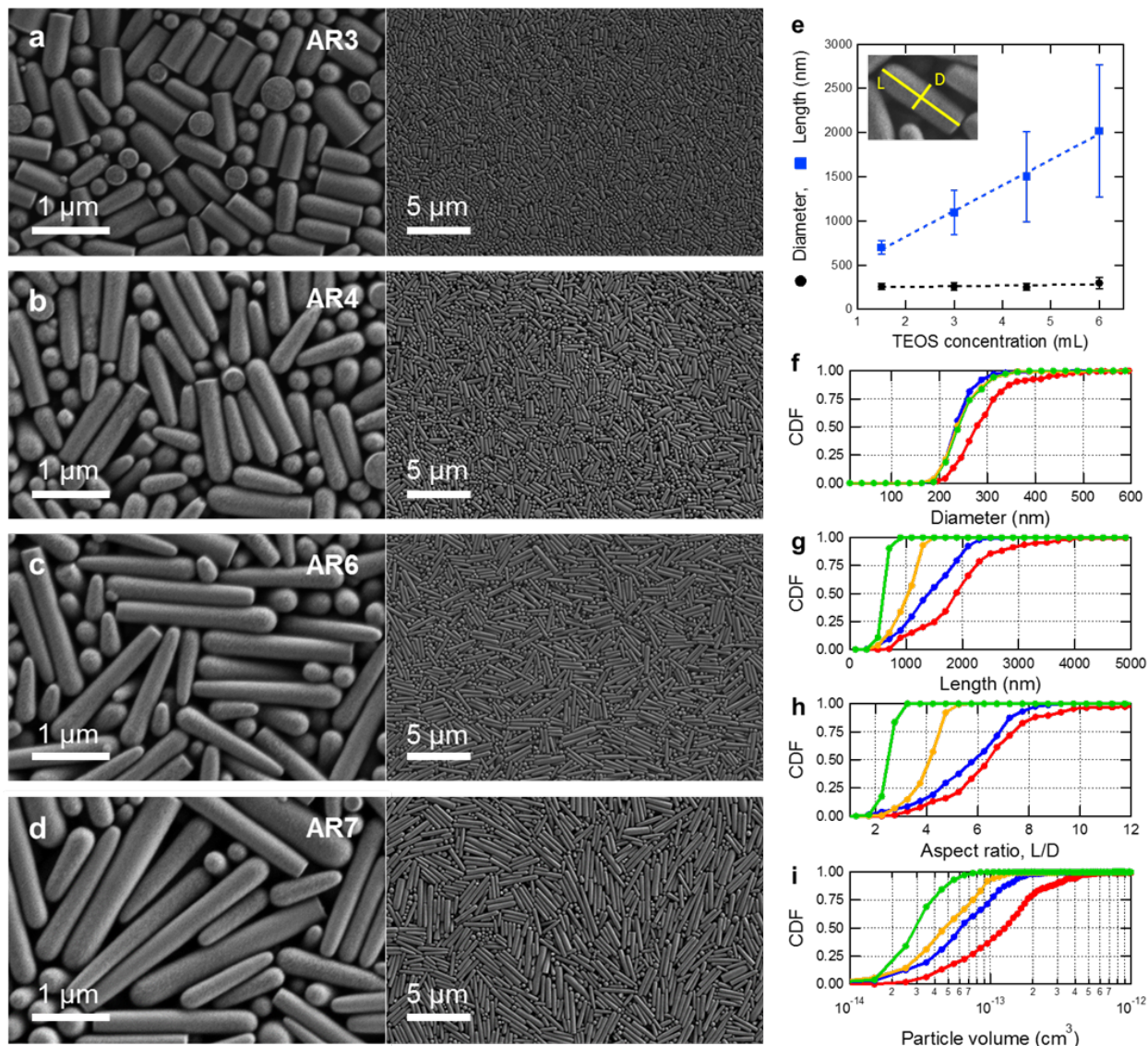
Figure 2. (a-d) SEM images at high and low magnifications of coated silica rods (adhesive hard rods) with varying aspect ratio and TEOS addition per batch for (a) 1.5 mL, (b) 3 mL, (c) 4.5 mL, and (d) 6 mL of TEOS. (e) Average diameter D (black circles) and average end-to-end length L (blue squares) as a function of TEOS addition. Error bars indicate the standard deviation in diameter (σ_D) and length (σ_L). (f-i) Cumulative probability distribution functions of the (f) diameter, (g) length, (h) aspect ratio, and (i) particle volume based on the average SEM dimensions

and assuming the shape was a hemispherocylinder. Symbols correspond to coated silica rods for AR3 (green), AR4 (orange), AR6 (blue), and AR7 (red).

Particle sizing from SEM measurements revealed a consistent average diameter D (250-300 nm) and standard deviation σ_D (30-70 nm) that did not vary significantly with TEOS addition, as shown in Fig. 2e and 2f. Meanwhile, the average length L and standard deviation in length σ_L increased linearly with increasing TEOS concentration (Fig. 2e and Fig. 2g). The corresponding average particle aspect ratio AR increased from approximately 3 to 7 with increasing TEOS addition (Fig. 2h). The trends in rod dimensions and polydispersity reported here ($\sigma_D/D \sim 0.14$-0.17, $\sigma_L/L = 0.11$-0.23, $\sigma_{AR}/AR = 0.11$-0.17) were generally consistent at lower TEOS additions (1.5 mL and 3 mL) with measurements reported by Kuijk et $al.$[9] However, the length distribution and corresponding aspect ratio distribution broadened considerably at higher TEOS additions, namely when adding 4.5 mL or 6 mL of TEOS ($\sigma_L/L = 0.34$-0.37, $\sigma_{AR}/AR = 0.27$-0.31). By estimating the particle volume using dimensions from SEM and assuming a hemispherocylinder shape, the resulting distribution in particle volume exhibited a log-normal dependence, as demonstrated in the cumulative distribution function in Fig. 2i (see Supporting Information Fig. S1 for further details). The larger polydispersity in length and aspect ratio at higher TEOS additions was likely due to a greater propensity for termination of rod growth, as well as differences in the effectiveness of fractionation steps used to separate shorter rods by centrifugation. In principle, the polydispersity in the length and aspect ratio could be reduced further by additional fractionation and centrifugation steps, but with further loss in yield.

Several unique geometric features of these particles are worth noting. One intriguing feature is the asymmetry imparted by the distinct flat-end on one end of the rod. For attractive colloidal

systems, the planar geometry of the flat-end of the rod introduces a large contact area ($\sim D^2$), possibly enabling significantly stronger attractions compared to the hemispherical end-to-end contacts ($\sim D$). Furthermore, the flat end has been exploited to impart unique functionality in growing PMMA[21] or gold[20] to create Janus-type silica colloids. In addition to the particle-end asymmetry, different orientations for rod-rod contacts such as parallel ($\sim D^{1/2}L$) or crossed ($\sim D$) configurations would also be expected to introduce strong short-range attractions due to the geometric dependence of van der Waals forces.

A tapering effect of the rod diameter along the length-axis was also observed, for shorter rods in particular, as was reported previously.[11, 22] Rod tapering is hypothesized to occur either from the slow shrinking of the terminal aqueous droplet or from competing growth in the radial axis.[22] The particle sizing performed herein reported the diameter at the midpoint along the length axis to average tapering effects.

Lastly, SEM images showed particle alignment after drop-casting and drying on a flat surface. Orientation of silica rods upon drop-casting onto a flat surface was reported previously, and alignment was shown to be enhanced by applying shear.[11] Here, silica rods with larger aspect ratio (AR6 in Fig. 2c and AR7 in Fig. 2d) qualitatively showed greater alignment than lower aspect ratios as anticipated (AR3 in Fig. 2a and AR4 in Fig. 2b). The qualitative dependence of particle alignment on the aspect ratio could be rationalized based on the lower theoretical limit for the existence of liquid crystal nematic phases (L/D > 4.7) and smectic phases (L/D > 4.1) for monodisperse hard spherocylinders.[10, 41]

3.2 Octadecyl-brush coating

It was found that successful coating of the silica surface with an octadecyl-brush layer required the removal of residual organics remaining after washing and separation of the bare rods.

Thermogravimetric analysis of bare silica rods showed a significant loss in mass (8-12 wt%) upon heating from 120 °C to 500 °C (after dehydration at 120 °C), as shown in Fig. 3a. This degradation is primarily from residual PVP entrapped within the porous silica network as shown by comparison to thermal degradation of neat PVP. Thermal degradation of bare rods commenced near 200 °C, followed by more significant degradation between 300 °C to 500 °C. Other TGA measurements, elemental analysis, and ^{13}C NMR measurements have strongly suggested the presence of entrapped PVP within bare rods.[42] Some residual organic mass could also be due to entrapped citrate, as suggested from a carbon signal from TEM elemental mapping.[22] Nevertheless, it was shown that entrapped PVP or other material could be removed from the bare silica rods by calcination at 500 °C for 5 h, as shown by the significantly smaller mass loss (0.7 - 1.7 wt%) for calcined particles shown in Fig. 3a and Table 1. The separation can be achieved without fusion between adjacent silica surfaces, which can occur at higher temperatures near 900 °C,[43] such that calcined rods could be successfully resuspended in ethanol and water.
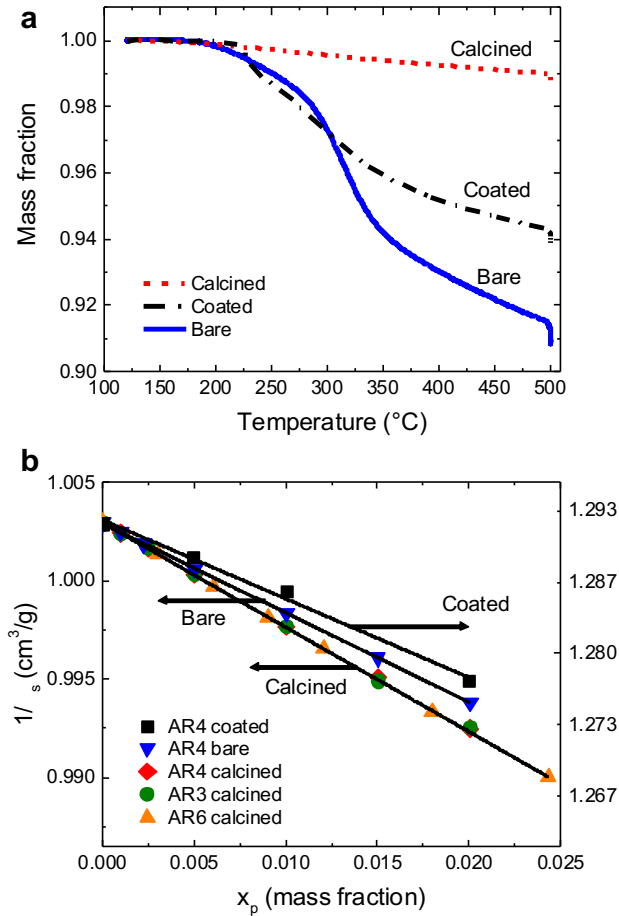
Figure 3. (a) Thermogravimetric analysis of bare (blue solid line), calcined (red dashed line), and coated silica rods (black dash-dotted line) for sample AR4 shows the mass fraction as a function of temperature from 120 °C to 500 °C, after dehydration at 120 °C. The total mass loss for each sample is summarized in Table 1. (b) The inverse of the suspension density as a function of particle mass fraction for the bare and calcined AR3, AR4, and AR6 samples suspended in water (left axis) and the coated AR4 sample suspended in cyclohexane (right axis) measured at 25.0 °C. The particle densities for the bare, calcined, and coated silica rods were determined from the best fit line (solid black lines) in relation to Eq. (3).

The surface coating coverage of octadecyl-brush chains was estimated using Eq. (2) based on the TGA mass loss and the BET surface area (Table 1). In general, the mass loss of coated rods ranged between 4-6 wt%, which corresponded to an estimated 0.9-1.4 chains/nm^2 for the examined aspect ratios. The coating coverage on silica rods was in good agreement with the coating coverage determined previously for silica spheres having 1-2 chains/nm^2.[28] This estimate was a lower-bound as it assumed full coverage of the accessible surface area based nitrogen adsorption measurements. However, a gradient in coating coverage could exist from confinement effects and lower accessibility of chains within the internal porous structure. A physically unrealistic upper-bound estimate for the coating coverage was 13-16 chains/nm^2 using the external geometric surface area of the rods determined from SEM and assuming a hemispherocylinder shape. This unrealistic upper-bound estimate was a strong indication that a large fraction (89-94%) of the grafted octadecyl-brush must penetrate and coat the internal pores of the silica particles. The presence of the grafted brush layer within the particle interior also suggests that the pore volume is approximately 9-12 vol% of the total particle volume.

The particle skeletal density was determined for the bare, calcined, and coated silica rods for sample AR4, as shown in Fig. 3b. The AR4 bare sample had a skeletal density of 1.82 ± 0.01 g/cm^3, which was in fair agreement with the density determined from previous reports using density matching solvent mixtures (1.90 ± 0.03 g/cm^3).[9] Upon calcination, the skeletal density increased to 2.08 ± 0.01 g/cm^3, which was in better agreement with the density of amorphous silica spheres (~2.2 g/cm^3).[3] The removal of entrapped PVP within bare rods by calcination would be expected to increase the skeletal density. Furthermore, the BET surface area of AR4 bare silica sample (64 m^2/g) was found to increase after calcination (128 m^2/g), likely due to exposing additional surface area within the silica network by removing entrapped polymer. After coating

the calcined rods with an octadecyl-brush, the skeletal density decreased to 1.79 ± 0.14 g/cm^3 when suspended in cyclohexane. A decrease in the skeletal density with coating is expected based on the addition of a lower density octadecyl-brush layer (octadecane, 0.777 g/cm^3 fluid at 30 °C).[31] However, a portion of this reduction in skeletal density could also result from the formation of solvent-inaccessible pores within the silica rods after the coating procedure.

3.3 Surface roughness of silica rods

Surface roughness features of calcined silica rods were determined by plotting the surface profile along particle edges determined by TEM, as shown for a representative sample in Fig. 4. Roughness parameters including the root mean squared height and the maximum height deviation from the average profile height are shown in Fig. 4b and summarized in Table 1 for different samples. The root mean squared height ranged between 1-2 nm, while the maximum height deviation for each sample ranged between 3-5 nm. These surface roughness parameters are independent of the TEOS addition. This degree of roughness is consistent with the formation of smaller primary silica particles (~1-5 nm) that nucleate and agglomerate to grow the porous rod-shaped particle. The apparent surface roughness and porosity are also consistent with the large specific surface area determined from nitrogen adsorption measurements and BET analysis (70-140 m^2/g), which is approximately one order of magnitude larger than the geometric surface area of a hemispherocylinder using rod dimensions from SEM (7-9 m^2/g).
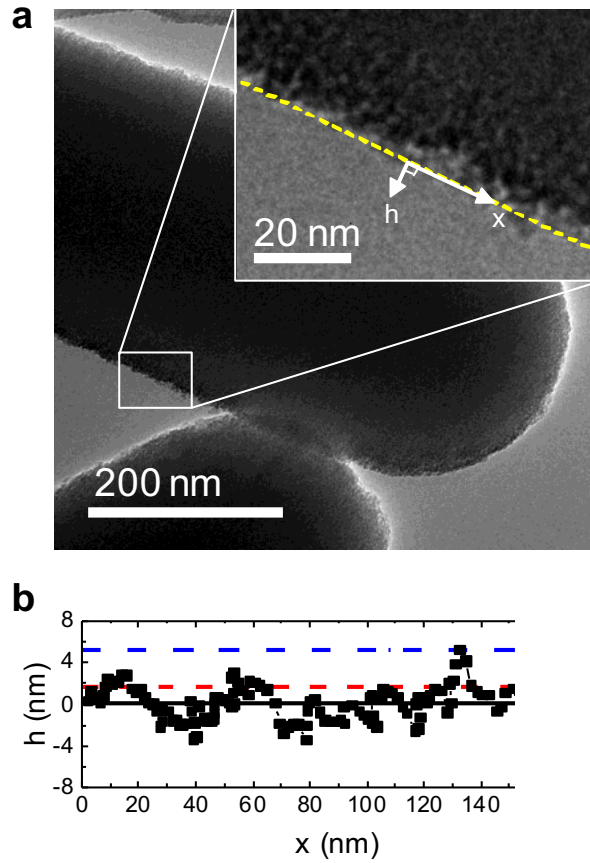
Figure 4. (a) A representative TEM image of calcined silica rods (AR4 calcined) that show surface roughness deviations along the length axis of the particle. (b) The surface profile height, h, as a function of the distance, x, along the particle edge. The surface roughness parameters including the maximum height (blue dash dot) and the root mean squared height (red dash) varied between 1-5 nm.

Surface roughness was shown previously to play an important role in mitigating the strength of attraction between colloids with short-range depletion interactions.[44, 45] In particular, surface roughness and asperities were shown to decrease the attraction strength by orders of magnitude for a system of platelet-shaped particles having short-range depletion attractions, in which a relatively

few number of asperities larger than the depletant size could significantly suppress the overlap volume.[44, 45] However, for the special case of commensurate or ordered surface roughness features, it was shown that the overlap volume and attractions between surfaces could be enhanced.[44] We propose that similar surface roughness effects could affect the short-range attractions and physical bonds formed between octadecyl-coated silica rods by decreasing the accessible contact area upon the close approach of rod surfaces. The attraction range for such systems is anticipated to occur at silica surface-surface separation distances of approximately 2-4 nm based on the length scale of octadecyl-chains in the fluid-state and solid-state.[3, 27] The effect of surface roughness is not currently understood for short-range attractive systems induced by a surface-freezing and melting transitions between the brush layer and surrounding linear alkane solvent. The similarity between the length scales of the surface roughness and the range of attraction warrants future investigation into these effects.

3.4 Scattering of calcined and coated silica rods

Ultra-small angle X-ray scattering (USAXS) measurements on dilute suspensions were performed to compare the particle form factors in solution with the particle dimensions obtained from microscopy on dried samples, and to examine the attractive nature of coated silica rods when suspended in tetradecane. USAXS methods are able to probe a wide range of relevant length scales from ~6 μm to ~6 nm by collecting scattered intensity over a broad q-range from 0.0001 Å^{-1} < q < 0.1 Å^{-1}. Scattering of dilute suspensions of calcined silica rods in ethanol for varying aspect ratios are shown in Fig. 5a, where the individual spectra are vertically offset for clarity. In general, scattering curves of hard rods showed slight increases in intensity at low-q (0.0001-0.001 Å^{-1}) with increasing aspect ratio and subtle deviations in intensity within

intermediate q-range (0.001-0.01 Å^{-1}). These qualitative trends were consistent with SEM

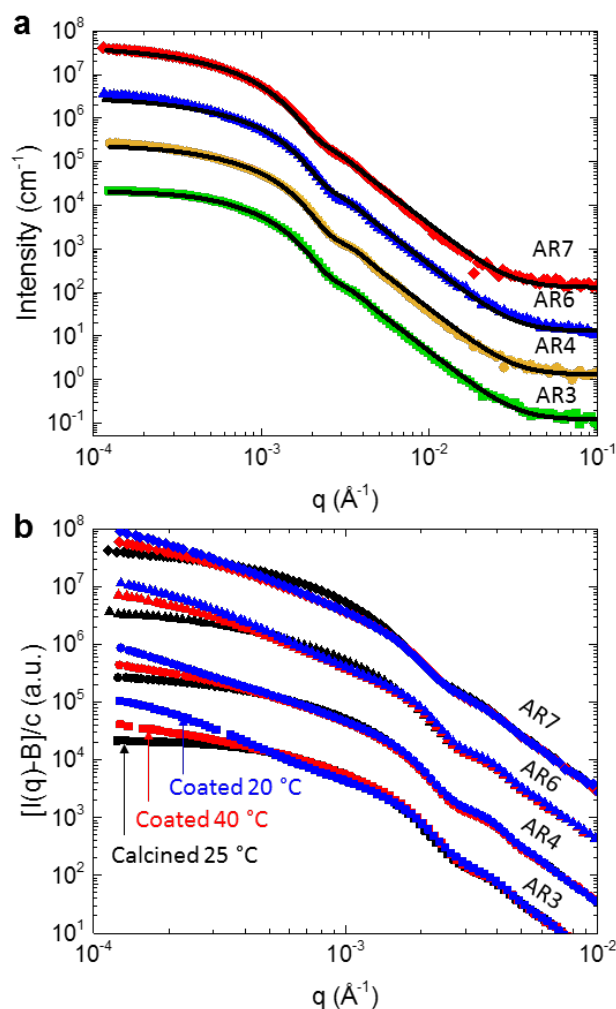measurements that revealed rods with similar diameters, but with varying lengths.

Figure 5. (a) USAXS scattering curves of the slit-smeared scattered intensity as a function of the

scattering vector (q) for dilute suspensions of calcined silica rods synthesized with varying TEOS

additions (bottom to top) 1.5 mL (AR3, green squares), 3 mL (AR4, orange diamonds), 4.5 mL

(AR6, blue triangles), and 6 mL (AR7, red diamonds). The best fits using a polydisperse cylinder

form factor model are also shown (solid black lines). The cylinder model parameters D, L, and

corresponding standard deviations are summarized in Table 1. (b) Normalized USAXS scattering

curves of dilute coated silica rods in tetradecane at 40 °C (red symbols) and 20 °C (blue symbols)

for samples AR3, AR4, AR6, AR7 (bottom to top). The corresponding scattering pattern of dilute

calcined silica rods in ethanol at 25 °C is shown for comparison (black symbols). All scattering

curves and fits are shifted vertically by a factor of 1, 10, 100, and 1000 for clarity (bottom to top).

To quantify the dimensions of hard rods in solution, the experimental scattering curves were fit

with a polydisperse cylinder form-factor model using a Schulz distribution for the cylinder radius

and length,[35] as shown in Fig. 5a (solid black lines). The best-fit model parameters are summarized

in Table 1 including the number average D, L, and standard deviations that were obtained from

the polydispersity parameter (σ_L/L and σ_D/D). Fitting parameters and further details are provided

in the Supporting Information. Overall, the cylinder model displayed very good agreement with

diameters determined from SEM (D ~ 250-300 nm and σ_D ~ 50-70 nm). Furthermore, the

polydisperse cylinder model fit showed consistent trends with increasing L as a function of TEOS

addition. However, the best fit L parameters were consistently larger than determined from

microscopy. The quantitative discrepancy between L determined from scattering and microscopy

measurements could arise for several reasons, such as the greater sensitivity of USAXS to the

larger sizes in the distribution, the combined contributions of polydispersity in diameter and length,

and the presence of a relatively small number of larger rods. Overall, the dimensions determined

by USAXS and SEM were consistent within the polydispersity in both diameter and length

dimensions.

Coated silica rods dispersed in tetradecane showed qualitatively similar scattering at mid-q to

high-q (q > 0.003 Å^{-1}), with differences evident as an increase in scattered intensity at low-q

(q < 0.003 Å^{-1}, Fig. 5b). To better compare between samples, the incoherent background was

subtracted and the total intensity was normalized by a constant to the dilute calcined rods to

account for differences in concentration, scattering length density difference between the particles and solvent, and deviations in path length. The low-q upturn ($q < 0.0005$ Å^{-1}) upon cooling from 40 °C (red symbols) to 20 °C (blue symbols) relative to the calcined hard rods (black symbols) is a signature of an increase in the attraction strength between particles. The dilute, adhesive hard rods in tetradecane showed qualitatively similar behavior to adhesive hard spheres that also demonstrated a low-q upturn and increase in attraction strength upon cooling from 40 °C to 20 °C, as shown previously using small angle neutron scattering.[27] Future modeling efforts will focus on extracting a temperature-dependent strength of attraction from this data.

3.5 Rheology of AHR thermoreversible gels

A colloidal suspension consisting of octadecyl-coated silica rods dispersed in tetradecane exhibits thermoreversible gelation, as illustrated by rheological measurements reported in Fig. 6. This thermoreversible behavior was qualitatively similar to model systems composed of octadecyl-coated spheres in tetradecane[3, 27] or hexadecane.[25, 28] For these systems, sample temperature can be conveniently controlled to induce transitions between a fluid-like state at higher temperature (40 °C) and gel-like state at lower temperatures (20-30 °C). Furthermore, the sample shear history can be "erased" by thermal cycling to recover the initial fluid-like state between each rheological measurement. Due to the negligible brush thickness (1.85 nm in the gel-state and 2.1 nm in the fluid-state)[27] as compared to the core diameter and length, the particle aspect ratio varies by a negligible amount (< 0.01) when varying temperature. Subtle changes in the density of tetradecane with varying temperature also results in negligible changes of particle volume fraction (< 0.001) within 15 °C to 40 °C.[3]

Figure 6 shows thermoreversible gelation behavior for a suspension of the AR3 coated rods in tetradecane at a particle mass fraction of 64 wt% (41 vol%). As observable in Fig. 6a, the

28

suspension displayed more fluid-like behavior at 40 °C and gel-like behavior at 20 °C by forming a self-supporting gel. Small-amplitude oscillatory shear measurements of the same sample undergoing a temperature ramp between 35 °C and 15 °C at 1 °C/min are shown in Fig. 6b. At higher temperatures the suspension exhibited more fluid-like character with the loss modulus being greater than the storage modulus (G" > G'). A crossover occurred at 29 °C such that G' > G" upon cooling the sample, which signified a transition to a gel-like state. Cooling the sample further below the crossover temperature showed a large increase in the dynamic moduli by nearly five orders of magnitude (~0.5 Pa to 50,000 Pa). The reverse trend was found upon heating the same sample, which confirmed thermoreversible behavior. A slight hysteresis in the cooling and heating curves was apparent, and it was shown previously to depend on sample aging effects and the temperature ramp rate for adhesive hard sphere systems.[3]
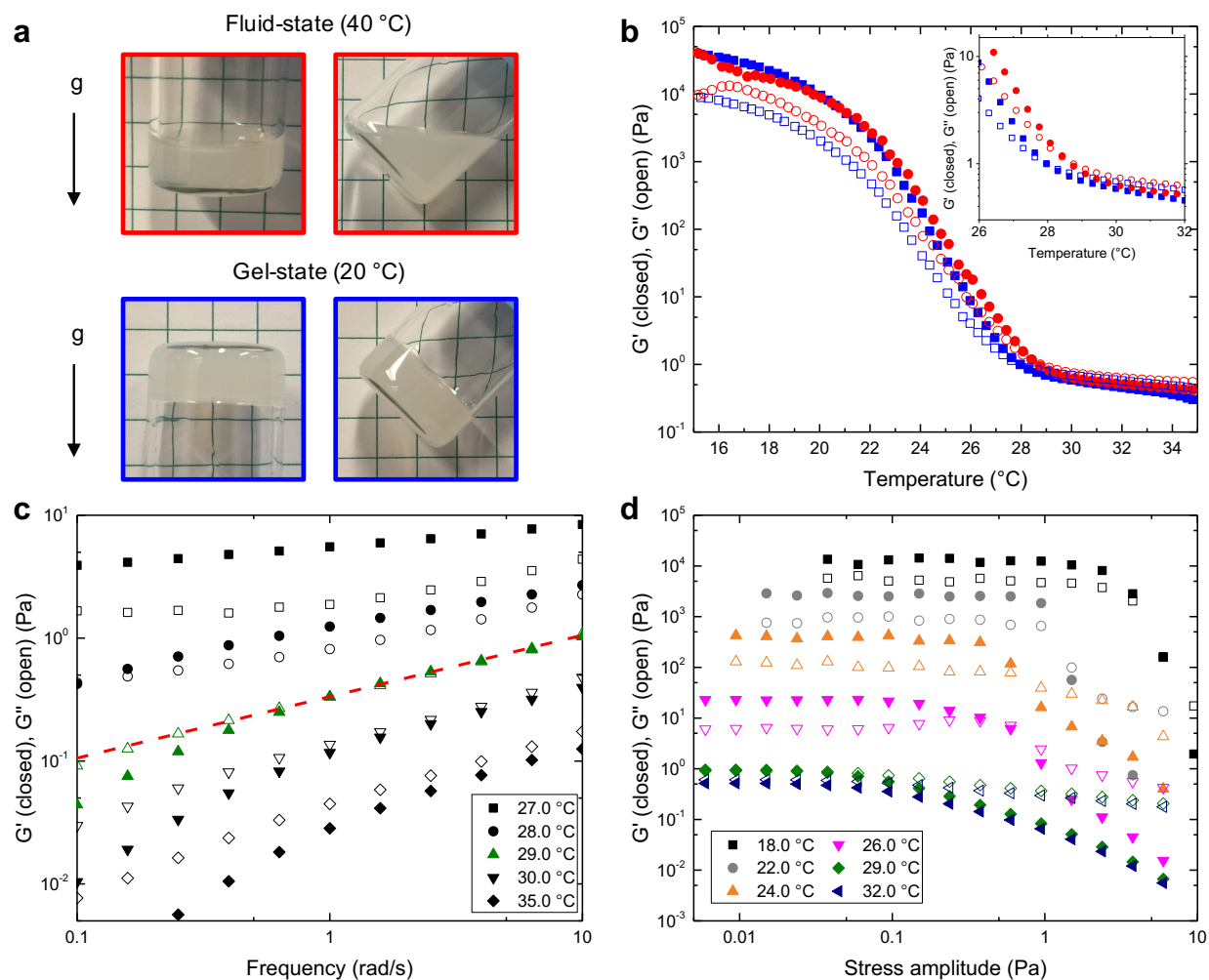
Figure 6. (a) Images of adhesive hard rods suspended in tetradecane (AR3 coated, 64 wt%, 41 vol%) in a fluid-like state at 40 °C (top) and gel-like state at 20 °C (bottom). (b) Small amplitude oscillatory shear measurements showing the storage modulus (G', closed symbols) and loss modulus (G", open symbols) for the same AHR suspension as a function of temperature (1 °C/min ramp rate, $\sigma_0 = 0.03$ Pa, $\omega = 1$ Hz) in the cooling direction (blue circles) and heating directions (red squares). The thermal cycling between a fluid-like state and a gel-like state signified thermoreversible gelation behavior. (c) Frequency sweeps at a fixed temperature ranging between 27 °C to 35 °C (top to bottom) and a constant stress amplitude ($\sigma_0 = 0.03$ Pa)

showed a critical gel transition temperature (29.0 °C) defined where G' ~ G'' ~ ω^n with a scaling

exponent n = 0.5 (dashed red line). For clarity, G' and G'' were vertically shifted by a factor of

1.5, 1.5, 1, 0.5, 0.25 for temperatures 27, 28, 29, 30, 35 °C, respectively. (d) Amplitude sweeps

at fixed frequency (1 Hz) and constant temperature ranging between 18 °C to 32 °C (top to bottom)

showed the transition from the linear viscoelastic regime.

The critical gelation temperature was identified using the Winter-Chambon criterion in which

the storage and loss modulus scale with frequency as G' ~ G'' ~ ω^n, with the scaling exponent

n = 0.5 over a broad frequency range.[46] Figure 6c shows frequency sweeps in the linear viscoelastic

regime at different temperatures for the same AR3 sample at 64 wt%. At 29 °C, a power-law

dependence in frequency for G' and G'' was found with an exponent n = 0.5 over a broad frequency

range, shown as the dashed red line in Fig. 6c. Above the critical temperature, the sample exhibited

more liquid-like behavior with G'' > G', and conversely below the critical temperature exhibited

more solid-like behavior with G' > G'' over a broad range in frequency. Figure 6d shows the

change in G' and G'' at varying stress amplitudes with a constant temperature and a fixed frequency

of 1 Hz. The transition out of the linear viscoelastic regime occurred at relatively low stress

amplitudes, which strongly depended on the sample temperature. The onset stress amplitude was

found to decrease from 5 Pa to 0.1 Pa with increasing temperature from 18 to 32 °C.

The estimated rotational diffusivity (D_{rot}) and translational diffusivity (D_{trans}) of dilute, non-

interacting, silica rods at 20 °C range between D_{rot} ~ 3 s^{-1} to 0.3 s^{-1} and D_{trans} ~ 4×10^{-13} m^2/s to $2\times10^{-}$

^{13} m^2/s for the AR3 and AR7 samples, respectively.[47] The corresponding dimensionless rotational

Péclet numbers ($Pe_r = \dot{\gamma}/D_{rot}$) are Pe_r < 0.005 to 0.06, using the shear rate $\dot{\gamma} = \gamma_0\omega$ with a strain

amplitude $\gamma_0 = 0.01$ and the highest frequency $\omega = 10$ rad/s. If we introduce an effective sphere

radius (a) as a characteristic distance for diffusion, then the Péclet numbers ($Pe = a^2\dot{\gamma}/D_{trans}$)

are Pe < 0.002 to 0.008. In all cases examined here in which $Pe_r < 1$ and $Pe < 1$, Brownian motion

will tend to randomize particle rotations or particle displacements faster than the imposed flow

will tend to align rods along the flow direction. In general, $Pe_r > 1$ when the shear rate exceeds 3

to 0.3 s^{-1}, and $Pe > 1$ when the shear rate exceeds 9 to 2 s^{-1}. The corresponding Deborah numbers

($De_r = \omega/D_{rot}$ and $De = a^2\omega/D_{trans}$) range from $0.005 < De_r < 6$ and $0.002 < De < 0.8$ for low aspect

ratio and frequency (AR3, 0.1 rad/s), and high aspect ratio and frequency (AR7, 10 rad/s),

respectively. Within the frequency range $1 < \omega < 10$ rad/s, the timescale probed during the

rheological response transitions from a timescale that is greater than the characteristic timescale

for rotational diffusion ($\omega^{-1} > D_{rot}^{-1}$), to a timescale that is less than rotational diffusion ($\omega^{-1} < D_{rot}^{-1}$).

The particle Reynolds numbers ($Re_p = \dot{\gamma}a^2\rho/\eta$) remain very small ($10^{-9}$) for all aspect ratios such

that effects of particle inertia can be neglected.

An order of magnitude estimate of the bond strength between particles in the fluid-like state and

gel-like state can be based on the measured storage modulus, particle volume fraction, and average

particle volume. Assuming the total "stored" energy in a sample pertains only to energy stored

between particle bonds, the total stored energy E would scale as $E \sim VG' \sim nZb \sim \varphi VV_p^{-1}Zb$. Here,

V is the sample volume, G' is the storage modulus, n is the number of particles per volume, Z is

the average number of bonds per particle, b is the energy per bond, φ is the particle volume

fraction, and V_p is the average particle volume determined from SEM measurements. Rearranging

gives a rough estimate of the bond energy as $b \sim G'V_p\varphi^{-1}Z^{-1}$. Assuming an average number of

bonds per particle (Z = 6), this gives an estimate of b ~ 1 kT at 40 °C (T > T_{gel}), b ~ 4 kT at 29 °C

(T ~ T_{gel}), and b ~ 70 kT at 26 °C (T < T_{gel}). This estimate depends critically on the assumed

average bond number Z, among other generalizations. For example, b ~ 4 kT (T > T_{gel}) to 11 kT

$(T \sim T_{gel})$ if $Z = 2$. A better quantification of the bond strength will be extracted by simulation and modeling of the measured scattering intensity, as previously performed for AHS gels.[4, 29]

Further investigation into the rheology, gelation behavior, and gel microstructure of the adhesive hard rod system is ongoing with the goal of understanding dynamic arrest transitions as a function of aspect ratio, volume fraction, and temperature. Importantly, the transition temperature is higher than expected for similar concentrations of suspensions of spherical particles of comparable size, suggesting the aspect ratio may promote dynamic arrest.[30]

4. CONCLUSIONS

A model colloidal system of adhesive hard rods was developed with tunable aspect ratios and temperature-dependent interactions. The TEOS concentration was adjusted to control the particle aspect ratio during silica rod synthesis. Bare silica rods were calcined to remove residual entrapped polymer and then were grafted with an octadecyl-brush to introduce thermoreversible short-range attractions in tetradecane. The rod length and length polydispersity were found to increase with the TEOS addition, while other properties such as the rod diameter, diameter polydispersity, particle density, surface roughness, and coating coverage did not strongly depend on the initial TEOS concentration. Ultra-small angle X-ray scattering measurements performed on dilute suspensions of adhesive hard rods in tetradecane demonstrated that coated silica rods were attractive, as characterized by a low-q upturn in the scattered intensity. Finally, the rheology of a concentrated suspension of adhesive hard rods dispersed in tetradecane displayed a thermoreversible gelation, whereby the suspension showed a five order of magnitude change in dynamic moduli within the temperature range 15-40 °C. The adhesive hard rod model system serves as platform to explore the combined effects of particle shape anisotropy and attraction

strength on the dynamic arrest transitions for anisotropic colloidal suspensions with thermoreversible, short-range attractions.

ASSOCIATED CONTENT

Supporting Information. Details and equations of the form factor for polydisperse cylinders. (Fig. S1) Comparison of probability plots of coated silica rod volume for Log-normal, Normal, and Weibull distributions. (Table S1) Summary of USAXS fitting parameters using a polydisperse cylinder form factor model. (Table S2) USAXS background and normalization constants for coated silica rods. This material is available free of charge via the Internet at http://pubs.acs.org.

AUTHOR INFORMATION

Corresponding Author

*E-mail: wagnernj@udel.edu

Notes

The authors declare no competing financial interests.

ACKNOWLEDGMENT

34

REFERENCES

1.   Lu, P. J.; Zaccarelli, E.; Ciulla, F.; Schofield, A. B.; Sciortino, F.; Weitz, D. A. Gelation of particles with short-range attraction. *Nature* **2008,** *453* (7194), 499-503.

2.   Hsiao, L. C.; Solomon, M. J.; Whitaker, K. A.; Furst, E. M. A model colloidal gel for coordinated measurements of force, structure, and rheology. *J Rheol* **2014,** *58* (5), 1485-1504.

3.   Eberle, A. P. R.; Castañeda-Priego, R.; Kim, J. M.; Wagner, N. J. Dynamical Arrest, Percolation, Gelation, and Glass Formation in Model Nanoparticle Dispersions with Thermoreversible Adhesive Interactions. *Langmuir* **2011,** *28* (3), 1866-1878.

4.   Eberle, A. P. R.; Wagner, N. J.; Castañeda-Priego, R. Dynamical Arrest Transition in Nanoparticle Dispersions with Short-Range Interactions. *Phys Rev Lett* **2011,** *106* (10), 105704.

5.   Solomon, M. J.; Spicer, P. T. Microstructural regimes of colloidal rod suspensions, gels, and glasses. *Soft Matter* **2010,** *6* (7), 1391-1400.

6.   Wilkins, G. M.; Spicer, P. T.; Solomon, M. J. Colloidal system to explore structural and dynamical transitions in rod networks, gels, and glasses. *Langmuir* **2009,** *25* (16), 8951-9.

7.   Wierenga, A. M.; Philipse, A. P.; Lekkerkerker, H. N. W. Aqueous dispersions of colloidal boehmite: structure, dynamics, and yield stress of rod gels. *Langmuir* **1998,** *14* (1), 55-65.

8.   Reddy, N. K.; Zhang, Z.; Lettinga, M. P.; Dhont, J. K. G.; Vermant, J. Probing structure in colloidal gels of thermoreversible rodlike virus particles: Rheology and scattering. *J Rheol* **2012,** *56* (5), 1153-1174.

9.   Kuijk, A.; van Blaaderen, A.; Imhof, A. Synthesis of Monodisperse, Rodlike Silica Colloids with Tunable Aspect Ratio. *J Am Chem Soc* **2011,** *133* (8), 2346-2349.

10.   Kuijk, A.; Byelov, D. V.; Petukhov, A. V.; van Blaaderen, A.; Imhof, A. Phase behavior of colloidal silica rods. *Faraday Discuss* **2012,** *159*, 181.

11.   Xu, T.; Davis, V. A. Liquid crystalline phase behavior of silica nanorods in dimethyl sulfoxide and water. *Langmuir* **2014,** *30* (16), 4806-13.

12.   Liu, B.; Besseling, T. H.; van Blaaderen, A.; Imhof, A. Confinement Induced Plastic Crystal-to-Crystal Transitions in Rodlike Particles with Long-Ranged Repulsion. *Phys Rev Lett* **2015,** *115* (7), 078301.

13.   Liu, B.; Besseling, T. H.; Hermes, M.; Demirors, A. F.; Imhof, A.; van Blaaderen, A. Switching plastic crystals of colloidal rods with electric fields. *Nat Commun* **2014,** *5*, 3092.

14.   Kuijk, A.; Troppenz, T.; Filion, L.; Imhof, A.; van Roij, R.; Dijkstra, M.; van Blaaderen, A. Effect of external electric fields on the phase behavior of colloidal silica rods. *Soft Matter* **2014,** *10* (33), 6249-55.

15.   Datskos, P.; Sharma, J. Synthesis of segmented silica rods by regulation of the growth temperature. *Angew Chem Int Ed Engl* **2014,** *53* (2), 451-4.

16.   Datskos, P.; Chen, J.; Sharma, J. Addressable morphology control of silica structures by manipulating the reagent addition time. *RSC Adv* **2014,** *4* (5), 2291-2294.

17.   Yang, Y.; Chen, G.; Martinez-Miranda, L. J.; Yu, H.; Liu, K.; Nie, Z. Synthesis and Liquid-Crystal Behavior of Bent Colloidal Silica Rods. *J Am Chem Soc* **2015**.

18.   Datskos, P.; Cullen, D. A.; Sharma, J. Step-by-Step Growth of Complex Oxide Microstructures. *Angew Chem Int Ed Engl* **2015,** *54*, 9011-9015.

19.   Datskos, P.; Chen, J.; Sharma, J. Synthesis of very small diameter silica nanofibers using sound waves. *Chem. Commun.* **2014,** *50* (55), 7277-9.

20.   Chaudhary, K.; Chen, Q.; Juarez, J. J.; Granick, S.; Lewis, J. A. Janus colloidal matchsticks. *J Am Chem Soc* **2012,** *134* (31), 12901-3.

21.   Peng, B.; Soligno, G.; Kamp, M.; de Nijs, B.; de Graaf, J.; Dijkstra, M.; van Roij, R.; van Blaaderen, A.; Imhof, A. Site-specific growth of polymers on silica rods. *Soft Matter* **2014,** *10* (48), 9644-50.

22.   Longbottom, B. W.; Rochford, L. A.; Beanland, R.; Bon, S. A. Mechanistic Insight into the Synthesis of Silica-Based "Matchstick" Colloids. *Langmuir* **2015,** *31* (33), 9017-25.

23.   Van Helden, A. K.; Jansen, J. W.; Vrij, A. Preparation and characterization of spherical monodisperse silica dispersions in nonaqueous solvents. *J Colloid Interface Sci* **1981,** *81* (2), 354-368.

24.   Verduin, H.; Dhont, J. K. G. Phase diagram of a model adhesive hard-sphere dispersion. *J Colloid Interface Sci* **1995,** *172*, 425-437.

25.   Roke, S.; Berg, O.; Buitenhuis, J.; van Blaaderen, A.; Bonn, M. Surface molecular view of colloidal gelation. *Proc Natl Acad Sci U S A* **2006,** *103* (36), 13310-4.

26.   Grant, M.; Russel, W. Volume-fraction dependence of elastic moduli and transition temperatures for colloidal silica gels. *Phys Rev E* **1993,** *47* (4), 2606-2614.

27.   Eberle, A. P. R.; Wagner, N. J.; Akgun, B.; Satija, S. K. Temperature-Dependent Nanostructure of an End-Tethered Octadecane Brush in Tetradecane and Nanoparticle Phase Behavior. *Langmuir* **2010,** *26* (5), 3003-3007.

28.   Roke, S.; Buitenhuis, J.; Miltenburg, J. C. v.; Bonn, M.; Blaaderen, A. v. Interface–solvent effects during colloidal phase transitions. *J Phys Condens Matter* **2005,** *17* (45), S3469-S3479.

29.   Valadez-Pérez, N.; Liu, Y.; Eberle, A.; Wagner, N.; Castañeda-Priego, R. Dynamical arrest in adhesive hard-sphere dispersions driven by rigidity percolation. *Phys Rev E* **2013,** *88*, 060302(R).

30.   Kim, J. M.; Fang, J.; Eberle, A. P. R.; Castañeda-Priego, R.; Wagner, N. J. Gel Transition in Adhesive Hard-Sphere Colloidal Dispersions: The Role of Gravitational Effects. *Phys Rev Lett* **2013,** *110* (20), 208302.

31.   Lide, D. R. *CRC Handbook of Chemistry and Physics*; 85th ed.; CRC Press: New York, 2004.

32.   Ilavsky, J.; Jemian, P. R.; Allen, A. J.; Zhang, F.; Levine, L. E.; Long, G. G. Ultra-small-angle X-ray scattering at the Advanced Photon Source. *J Appl Crystallogr* **2009,** *42* (3), 469-479.

33.   Ilavsky, J. Nika: software for two-dimensional data reduction. *J Appl Crystallogr* **2012,** *45* (2), 324-328.

34.   Ilavsky, J.; Jemian, P. R. Irena: tool suite for modeling and analysis of small-angle scattering. *J Appl Crystallogr* **2009,** *42* (2), 347-353.

35.   Kline, S. R. Reduction and analysis of SANS and USANS data using IGOR Pro. *J Appl Crystallogr* **2006,** *39* (6), 895-900.

36.   Guinier, A.; Fournet, G. *Small-Angle Scattering of X-rays*; John Wiley and Sons: New York, 1955.

37.   SasView. http://www.sasview.org/.

38.   Brunauer, S.; Emmett, P. H.; Teller, E. Adsorption of Gases in Multimolecular Layers. *J Am Chem Soc* **1938,** *60* (2), 309-319.

39.   Stober, W.; Fink, A.; Bohn, E. Controlled Growth of Monodisperse Silica Spheres in the Micron Size Range. *J Colloid Interface Sci* **1968,** *26*, 62-69.

40.   van Blaaderen, A.; van Geest, J.; Vrij, A. Monodisperse colloidal silica spheres from tetraalkoxysilanes: particle formation and growth mechanism. *J Colloid Interface Sci* **1992,** *154*, 481-501.

41.   Bolhuis, P.; Frenkel, D. Tracing the phase boundaries of hard spherocylinders. *J Chem Phys* **1997,** *106* (2), 666-687.

42.   Kuijk, A.; Imhof, A.; Verkuijlen, M. H. W.; Besseling, T. H.; van Eck, E. R. H.; van Blaaderen, A. Colloidal Silica Rods: Material Properties and Fluorescent Labeling. *Part Part Syst Charact* **2014,** *31* (6), 706-713.

43.   Zhuravlev, L. T. The surface chemistry of amorphous silica. Zhuravlev model. *Colloids Surf A Physicochem Eng Asp* **2000,** *173*, 1-38.

44.   Zhao, K.; Mason, T. G. Suppressing and enhancing depletion attractions between surfaces roughened by asperities. *Phys Rev Lett* **2008,** *101* (14), 148301.

45.   Zhao, K.; Mason, T. G. Directing colloidal self-assembly through roughness-controlled depletion attractions. *Phys Rev Lett* **2007,** *99* (26), 268301.

46.   Winter, H. H.; Chambon, F. Analysis of Linear Viscoelasticity of a Crosslinking Polymer at the Gel Point. *J Rheol* **1986,** *30* (2), 367-382.

47.   Tirado, M. M.; Martínez, C. L.; de la Torre, J. G. Comparison of theories for the translational and rotational diffusion coefficients of rod-like macromolecules. Application to short DNA fragments. *J Chem Phys* **1984,** *81* (4), 2047-2052.

TOC GRAPHIC